

# 3 The Physics of Quantum Impurity Models

Jan von Delft

Arnold Sommerfeld Center for Theoretical Physics

Ludwig-Maximilians-Universität München

Theresienstr. 37, 80333, Munich

## Contents

<b>1</b>	<b>Introduction</b>	<b>2</b>
<b>2</b>	<b>Single-impurity Anderson model: local moment formation</b>	<b>3</b>
<b>3</b>	<b>Kondo model: spin-exchange interaction</b>	<b>5</b>
<b>4</b>	<b>Numerical renormalization group</b>	<b>8</b>
<b>5</b>	<b>NRG results for the single-impurity Anderson model</b>	<b>12</b>
<b>6</b>	<b>Two-channel Kondo model</b>	<b>17</b>
<b>A</b>	<b>Schrieffer-Wolff transformation</b>	<b>19</b>

# 1 Introduction

A *quantum impurity model* describes a localized, discrete quantum system, the *impurity*, coupled to noninteracting excitations with a continuous (non-discrete) excitation spectrum, the *bath*. Such models were first invoked in the 1960s to explain certain anomalies in the resistivity of magnetic alloys, where the impurities are localized magnetic moments (or localized spins, for short). In subsequent decades, quantum impurity models turned out to be relevant in several other contexts, including transport through quantum dots and nanotubes, whose discrete energy levels act as impurities; dissipation and decoherence of qubits, described as impurities coupled to bosonic baths; and dynamical mean field theory, where a single lattice site is viewed as an impurity coupled to a self-consistently determined bath. This lecture aims to introduce the physics of quantum impurity models from a renormalization group perspective. By way of introduction, we begin with some historical remarks.

In 1934, de Haas, de Boer and van den Berg [1] discovered an unexpected phenomenon when measuring the resistance of gold as a function of temperature,  $\rho(T)$ : it showed a *minimum* at  $T = 3.70$  K, whereas it had been expected that the resistance would decrease monotonically with decreasing temperature as phonons freeze out, reaching its smallest value at  $T = 0$ . The fact that  $\rho(T)$  instead turns upward once  $T$  drops below 3.70 K indicates that in this regime the electron scattering rate increases with decreasing temperature—a finding that was very surprising at the time. In subsequent years, similar resistance minima were found in numerous so-called dilute magnetic alloys: metals such as Cu, Ag, Au containing a small concentration of magnetic impurities such as Cr, Mn, Fe.

The origin of the resistance minima observed for magnetic alloys remained puzzling until 1964, when Kondo offered an explanation [2]. He considered a model, since known as the *Kondo model*, describing a dilute concentration of localized spin-1/2 impurities immersed in a metallic conduction band, with a spin-exchange coupling between the localized spins and the conduction band. This coupling causes spin-flip scattering events: when a conduction electron scatters off a localized spin, the spin of both can flip. Kondo computed the corresponding scattering rate to lowest nontrivial order in the exchange coupling, and found that it *increases* with decreasing temperature, causing the resistance  $\rho(T)$  to likewise increase. This explained the resistance minimum.

Moreover, Kondo found that the scattering rate,  $\gamma(T)$ , increased *logarithmically* with decreasing  $T$ , like  $\ln(D/T)$ , where  $D$  is a large energy scale such as the bandwidth of the conduction band. This meant that while he had resolved an experimental puzzle, he had simultaneously discovered a theoretical one, which came to be known as the *Kondo problem*: what happens to the scattering rate in the limit  $T \rightarrow 0$ ? The perturbative result, implying a logarithmic divergence, clearly can not be trusted in this limit.

To answer this question, nonperturbative methods were called for. Over the years, a wide variety of approaches were applied to the Kondo problem, including the numerical renormalization group (NRG) [3, 4], the Bethe Ansatz [5, 6], conformal field theory [7], bosonization [8, 9], and Monte Carlo methods [10]. As a result, the answer to the above question is now very well

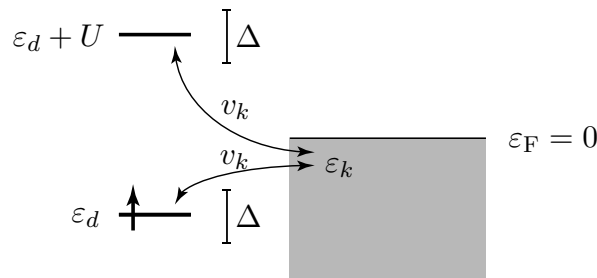
established: the scattering rate  $\gamma(T)$  approaches a constant value for  $T \rightarrow 0$ , because the local spin is *screened* by conduction electrons to form a *spin singlet*. The screened singlet acts just like a static (i.e. nonmagnetic) impurity, off which other electrons scatter very strongly, albeit without flipping their spin. The screening of a localized spin by conduction electrons has come to be known as the *Kondo effect*.

The crossover, with decreasing  $T$ , from an unscreened spin to a spin singlet is a paradigmatic example of a renormalization group (RG) flow between two RG fixed points. The goal of these notes is to elucidate the physics of quantum impurity models from such an RG perspective.

In the following sections, we will introduce two paradigmatic models describing spin screening: the single-impurity Anderson model and the Kondo model; explain why a perturbative treatment fails at low temperatures; describe Wilson’s numerical renormalization group approach for reaching low temperature; and discuss various physical quantities exhibiting signatures of spin screening. In the final section, we briefly discuss a model that does not show full spin screening—the two-channel Kondo model. We set  $\hbar = 1$  and  $k_B = 1$  throughout.

## 2 Single-impurity Anderson model: local moment formation

In 1961, P.W. Anderson introduced a “highly simplified” model, since known as the single-impurity Anderson model (SIAM), to explain the formation of local moments in magnetic alloys. In such systems, the magnetic impurities have  $d$  or  $f$  orbitals that are strongly localized, yet nevertheless hybridize with the host metal, in such a manner that they behave as localized spins (or magnetic moments) acting as dynamical degrees of freedom. A fully realistic description is very challenging, since  $d$  or  $f$  shells typically host several electrons, with strong local Coulomb interactions. Anderson argued that the essential physics could be captured by considering just a single, local level rather than an entire shell. He thus studied the Hamiltonian  $H_{\text{SIAM}} = H_{\text{bath}} + H_{\text{loc}} + H_{\text{hyb}}$ , with



$$H_{\text{bath}} = \sum_{ks} \varepsilon_k \hat{n}_{ks}, \quad \hat{n}_{ks} = c_{ks}^\dagger c_{ks}, \quad (1a)$$

$$H_{\text{loc}} = \sum_s \left( \varepsilon_d - \frac{1}{2} \hbar s \right) \hat{n}_{ds} + U \hat{n}_{d\uparrow} \hat{n}_{d\downarrow}, \quad \hat{n}_{ds} = d_s^\dagger d_s, \quad (1b)$$

$$H_{\text{hyb}} = \sum_{ks} v_k \left( c_{ks}^\dagger d_s + d_s^\dagger c_{ks} \right). \quad (1c)$$

Here,  $H_{\text{bath}}$  describes a band of free (noninteracting) electrons with spin  $s \in \{\uparrow, \downarrow\}$  and energy  $\varepsilon_k$  ( $k$  is a continuous momentum index),  $H_{\text{loc}}$  describes a discrete, localized level with energy  $\varepsilon_d$ , spin  $s$ , Zeeman splitting  $h$  if a magnetic field is applied (we set  $g\mu_B = 1$ ), and Coulomb energy cost  $U$  if the level is doubly occupied.  $H_{\text{hyb}}$  describes *hybridization* between the  $d$  level and the conduction band, allowing electrons to hop back and forth between the two with amplitude  $v_k$  (we choose it real and constant,  $v_k = v$ ). As a result, the  $d$  level acquires a finite width,  $\Delta$ . Since  $H_{\text{bath}}$  and  $H_{\text{hyb}}$  are quadratic, the conduction band can be integrated out, in principle. One then finds that the dependence of the  $d$  level dynamics on bath parameters enters only via the *hybridization function*

$$\Delta(\omega) = \sum_k \frac{v_k^2}{\omega - \varepsilon_k + i0^+}. \quad (2)$$

When this function is expressed through its spectral representation,  $\Delta(\omega) = \int d\epsilon \frac{\Gamma(\epsilon)}{\omega - \epsilon + i0^+}$ , the corresponding *hybridization spectrum* is given by

$$\Gamma(\epsilon) = \sum_k |v_k|^2 \delta(\epsilon - \varepsilon_k). \quad (3)$$

It characterizes how strongly a conduction band level with energy  $\epsilon$  couples to the impurity. Anderson assumed the hybridization spectrum to be constant near the Fermi energy; for concreteness, we will use the box-shaped form,

$$\Gamma(\epsilon) = (\Delta/\pi) \Theta(D - |\epsilon|), \quad \Delta/\pi = v^2\nu. \quad (4)$$

Here,  $D$  is the half-bandwidth of a flat band centered on the Fermi energy at  $\varepsilon_F = 0$ , related to the density of states per spin,  $\nu$ , by  $\nu = 1/(2D)$ , and  $\Delta$  is the width acquired by the  $d$  level through hybridizing with the bath. (This follows from Eq. (23) below.) Unless stated otherwise, we measure energy in units of  $D = 1$ .

The Hilbert space of the local level is spanned by four states,  $|0\rangle$ ,  $|\uparrow\rangle$ ,  $|\downarrow\rangle$ ,  $|\uparrow\downarrow\rangle$ , describing the local level being empty, occupied by one electron with spin  $\uparrow$  or  $\downarrow$ , or doubly occupied, respectively. They are eigenstates of  $H_{\text{loc}}$ , with eigenenergies  $E_0 = 0$ ,  $E_\uparrow = \varepsilon_d - \frac{1}{2}h$ ,  $E_\downarrow = \varepsilon_d + \frac{1}{2}h$ , and  $E_{\uparrow\downarrow} = 2\varepsilon_d + U$ , respectively. Unless stated otherwise, we will consider the case of zero magnetic field,  $h = 0$ . We are interested in the *local moment regime*, where the parameters are chosen such that the empty and doubly-occupied levels lie well above the (broadened) singly-occupied levels; this implies  $E_0 - E_s > \Delta$  and  $E_{\uparrow\downarrow} - E_s > \Delta$ , i.e.

$$\varepsilon_d + \Delta < 0, \quad \varepsilon_d + U > \Delta, \quad (5)$$

Then, the average occupancy of the local level,  $n_d = \sum_s \langle \hat{n}_{ds} \rangle$ , is  $\simeq 1$ . Thus, the  $d$  level hosts a local moment, containing a spin-up or down electron with equal probability,  $n_{d\uparrow} = n_{d\downarrow} \simeq \frac{1}{2}$ . Transitions between these two spin states can occur via second-order hopping processes involving  $|0\rangle$  or  $|\uparrow\downarrow\rangle$  as *virtual*, high-energy intermediate states. Their net result is that the spin on the

$d$  level has flipped from  $|\uparrow\rangle$  to  $|\downarrow\rangle$ , or vice versa, and a particle-hole excitation has been created in the band. The effective spin-flip rate due to such processes is found to be

$$J = \frac{v^2}{\varepsilon_d + U} - \frac{v^2}{\varepsilon_d} = -\frac{Uv^2}{\varepsilon_d(\varepsilon_d + U)} = -\frac{2U\Delta}{\pi\varepsilon_d(\varepsilon_d + U)}. \quad (6)$$

Note that  $J > 0$ , since in the local moment regime of Eq. (5),  $\varepsilon_d < 0$ . If one is interested only in the physics of these spin-flip processes, it is convenient to consider the Kondo model, which we discuss next.

### 3 Kondo model: spin-exchange interaction

The Kondo model (KM) is obtained from the SIAM by projecting the latter onto the subspace in which the local occupancy is strictly  $n_d = 1$ , i.e., only the impurity states  $|\uparrow\rangle$  and  $|\downarrow\rangle$  are considered, and focusing on the scattering of low-energy band excitations only. Formally, this can be achieved using a so-called Schrieffer-Wolff [11] transformation (outlined in App. A). Then, one obtains an effective Hamiltonian of the form  $H_{\text{KM}} = H_{\text{bath}} + H_{\text{spin}} + H_{\text{exchange}}$ , with

$$H_{\text{bath}} = \sum_{ks} \varepsilon_k \hat{n}_{ks}, \quad H_{\text{spin}} = h \hat{S}_d^z, \quad (7a)$$

$$H_{\text{exchange}} = J \hat{S}_d \cdot \hat{s}_c, \quad \hat{s}_c = \sum_{ks, k's'} c_{ks}^\dagger \frac{1}{2} \boldsymbol{\sigma}_{ss'} c_{k's'}. \quad (7b)$$

This defines the KM. Here,  $H_{\text{bath}}$  again describes a free conduction band;  $\hat{S}_d$  are spin- $\frac{1}{2}$  operators acting in the space spanned by  $|\uparrow\rangle$  and  $|\downarrow\rangle$ ; and  $\hat{s}_c$  are conduction band spin operators, describing its spin density at the impurity site. The local spin couples to the conduction electron spin density via an antiferromagnetic exchange interaction,  $J > 0$ , favoring an anti-alignment of the spins of the impurity and the conduction band. The KM describes the low-energy behavior of the SIAM, at energy scales for which charge fluctuations involving  $|0\rangle$  and  $|\uparrow\downarrow\rangle$  are “frozen out”, i.e., can occur only virtually.

The KM is an interesting model in its own right. It has been studied using a wide variety of theoretical methods, both analytical and numerical, and can be regarded as thoroughly understood. Below, we briefly summarize some of its salient properties. These will be elaborated in subsequent sections.

*Perturbative treatment:* When the KM is used to perturbatively compute the scattering rate of conduction electrons off the local spin in an expansion in powers of  $J$ , this rate is found to increase logarithmically with decreasing temperature,  $\gamma(T) \sim J + \nu J^2 \log(D/T)$ .

*Effective coupling:* The perturbation expansion can be expressed through an effective,  $T$ -dependent dimensionless coupling,  $g(T)$ , having the form

$$g(T) = \frac{1}{1/g_0 - \ln(D/T)}, \quad g_0 = \nu J. \quad (8)$$

At large temperatures,  $T \simeq D$ , the effective coupling reduces to its bare value,  $g_0$ . However, it increases with decreasing  $T$  due to the logarithm in the denominator.

*Kondo temperature:* When the temperature becomes sufficiently small, the perturbative correction is no longer small and the perturbative treatment breaks down (becomes invalid). The characteristic crossover scale at which this happens is called the Kondo temperature,  $T_K$ . One way of defining it is as the temperature at which the effective coupling diverges,  $g(T_K) = \infty$ , i.e., where the denominator in Eq. (8) vanishes,  $1/g_0 = \ln(D/T_K)$ . This yields

$$T_K \sim D e^{-1/(J\nu)}. \quad (9)$$

The Kondo temperature is exponentially small in the exchange coupling, reflecting the fact that  $g(T)$  depends logarithmically on  $T$ .

*Universality:* For  $T > T_K$ , the effective coupling can be expressed in the form

$$g(T) = \frac{1}{\ln(D/T_K) - \ln(D/T)} = \frac{1}{\ln(T/T_K)}. \quad (10)$$

( $g(T)$  is not defined for  $T < T_K$ , since its perturbative derivation becomes invalid.) This beautiful expression shows that the physics depends on the bare parameters of the model,  $J$ ,  $\nu$  and  $D$ , only in the combination  $T_K$ . When physical quantities, such as the resistivity or spin susceptibility are measured for different materials, or computed using different bare parameters, they will collapse onto a universal scaling curve when plotted as functions of  $T/T_K$ .

*Spin singlet ground state:* The regime  $T < T_K$  is beyond the reach of perturbative methods. However, the nature of the ground state can be anticipated from the fact that the effective coupling becomes large with decreasing temperature: the ground state will be such that the exchange interaction in the Hamiltonian,  $\hat{S}_d \cdot \hat{s}_e$ , is minimized. Consequently, the ground state of the KM is a spin singlet, i.e., has total spin  $S = 0$ .

*Kondo cloud:* The singlet ground state can be visualized as follows: A cloud of conduction electrons with a net spin of  $1/2$ , the so-called Kondo cloud, binds the local spin  $1/2$  into a singlet. Commonly used schematic depictions of this singlet include the following:

The singlet may be viewed as a bound state with binding energy  $T_K$ , albeit not a very tightly bound one: since  $T_K$  is an exponentially small energy scale, the spatial extent of the Kondo cloud scales is exponentially large, scaling as  $\xi_K \sim v_F/T_K$ , where  $v_F$  is the Fermi velocity.

*Spin screening:* The effect of the Kondo cloud on the local spin is called spin screening: by binding the local spin into a singlet, the cloud hides the presence of a local dynamical degree of freedom from the rest of the system. This has striking consequences for the temperature dependence of various physical quantities: as the temperature is decreased from above to below

$T_K$ , their behavior changes from reflecting the presence of a free spin to reflecting its absence (since it is screened into a singlet). Correspondingly,  $T \gg T_K$  is called the *local moment (LM) regime*, and  $T \ll T_K$  the *strong-coupling (SC) regime*.

We next discuss the leading  $T$  dependence of three physical quantities in these regimes: the impurity entropy  $S(T)$ , the impurity spin susceptibility  $\chi(T)$ , and the spin scattering rate,  $\gamma(T)$ . Corresponding numerical results will be shown in Sec. 5 when discussing the SIAM, whose low-energy behavior matches that of the KM.

*Impurity entropy:* The high- and low-temperature limits of the impurity entropy are given by

$$S(T) \simeq \begin{cases} \ln(2), & T \gg T_K, \\ \ln(1) = 0, & T \ll T_K. \end{cases} \quad (11)$$

These reflect the fact that the free, unscreened impurity has two degenerate states,  $|\uparrow\rangle$  and  $|\downarrow\rangle$ , whereas the ground state is a non-degenerate singlet.

*Spin susceptibility:* The static spin susceptibility, defined as the linear response of the local spin to an applied magnetic field, has the following limiting behaviors:

$$\chi(T) = \left. \frac{d\langle S_d^z(h) \rangle_T}{dh} \right|_{h=0} \simeq \begin{cases} \frac{1}{4T} \left( 1 - \mathcal{O}(\ln(T/T_K)) \right), & T \gg T_K, \\ \chi(0) \left( 1 - \mathcal{O}(T^2/T_K^2) \right), & T \ll T_K. \end{cases} \quad (12)$$

For high temperatures, it shows the Curie behavior,  $\chi(T) \sim 1/T$ , characteristic of a free spin, with logarithmic corrections reflecting the onset of spin screening. As spin screening becomes stronger with decreasing temperature, the Curie behavior is cut off, and for  $T \rightarrow 0$  the susceptibility approaches a constant, comparable in magnitude to  $1/T_K$ . In fact, this constant can be used to *define* the Kondo temperature, setting  $T_{K\chi} = 1/(4\chi(0))$  [4, 12]. (This definition has the advantage that it does not depend on bare parameters of the model. It differs from that of Eq. (9) by a constant of order unity, but that is no cause for concern, since the Kondo temperature in any case is a *crossover* scale, whose prefactor is a matter of convention.) A rough characterization of the crossover from high to low temperatures is provided by the Curie-Weiss expression  $\chi(T) \simeq 1/(4(T+T_{K\chi}))$ , but it should be recognized that this does not properly account for the leading high- and low- $T$  corrections indicated in Eq. (12).

*Electron scattering:* The rate at which conduction electrons scatter off the impurity has the limiting forms

$$\gamma(T) \sim \frac{1}{\ln(T/T_K)}, \quad T \gg T_K, \quad (13a)$$

$$\gamma(T) = \gamma(0) \left( 1 - \mathcal{O}(T/T_K)^2 \right), \quad T/T_K \ll 1. \quad (13b)$$

At high temperatures, it is simply proportional to the effective coupling,  $g(T)$ . Its logarithmic growth is cut off as screening sets in, and it approaches a constant as  $T \rightarrow 0$ .

*Fermi liquid behavior:* Once the local spin is fully screened into a singlet, the “remaining” conduction electrons scattering off it can no longer flip their spins; instead, they merely acquire

a phase shift. In this sense, the screened singlet acts as a static impurity, without any dynamics. However, it is a strong scatterer: for an electron incident at the Fermi energy, the phase shift acquired during scattering turns out to be  $\delta(\epsilon=0) = \pi/2$ , the maximum value possible for scattering off static impurities.

Nozières has developed a Fermi-liquid description [13] of the strong-coupling regime. It involves no dynamical impurity at all (since the latter is fully screened), only low-energy quasiparticle excitations, i.e., dressed versions of the original, bare conduction electrons of the KM. The quasiparticles experience mutual interactions that are weak and purely local, i.e., act only at the site of the screened impurity. The parameters of the Hamiltonian are fully determined by the energy dependence of the scattering phase shift,  $\delta(\epsilon)$ , and can be extracted from zero-temperature properties of the KM (which in turn are known exactly from a Bethe Ansatz solution [5, 6]). A perturbative treatment of these interactions readily yields the leading quadratic temperature dependence,  $(T/T_K)^2$ , indicated in Eqs. (12) for  $\chi(T)$  and (13a) for  $\gamma(T)$ . Fermi-liquid theory, combined with results from the exact Bethe Ansatz solution of the Kondo model [5, 6], can also be used to analytically derive the prefactors of the quadratic terms [14, 12], yielding

$$\frac{\chi(T)}{\chi(0)} - 1 = -0.821 \frac{T^2}{T_{K\chi}^2}, \quad \frac{\gamma(T)}{\gamma(0)} - 1 = -\frac{\pi^4}{16} \frac{T^2}{T_{K\chi}^2}, \quad T/T_{K\chi} \ll 1. \quad (14)$$

These prefactors are universal constants, characteristic of the strong-coupling regime of the KM. They serve as useful and stringent consistency checks for numerical treatments of the KM.

## 4 Numerical renormalization group

A description of the crossover from high to low temperatures, and of the strong-coupling regime, requires nonperturbative approaches [3–10]. Here, we focus on the numerical renormalization group (NRG), developed by Ken Wilson in 1975 as a specific implementation of his general RG ideas [3]. Although almost 50 years old, NRG remains the gold standard for solving quantum impurity models, due to its great flexibility, ability to resolve low-energy properties with high accuracy, and the insights it yields about the RG evolution of a system from high to low energies. Here, we discuss NRG for the example of the SIAM; since its low-energy behavior is governed by the Kondo model, the SIAM, too, exhibits a Kondo effect, with an exponentially small Kondo temperature. Hence, NRG results for the SIAM also serve to illustrate the physics for the KM discussed in the previous section. The SIAM was first treated with NRG by Krishna-murthy, Wilkens and Wilson in 1980 [15, 16]. For NRG reviews, see Refs. [4, 17].

Since the Kondo effect involves an exponentially small energy scale, Wilson’s goal was to devise a numerical scheme capable of resolving arbitrarily low energy scales. He achieved this goal by (i) discretizing the hybridization spectrum on a logarithmic grid that becomes arbitrarily dense around the Fermi energy; (ii) mapping the resulting discrete model onto a semi-infinite chain, called a *Wilson chain*, containing the impurity at the beginning and exponentially decaying hopping matrix elements along the chain; and (iii) diagonalizing this chain iteratively, while

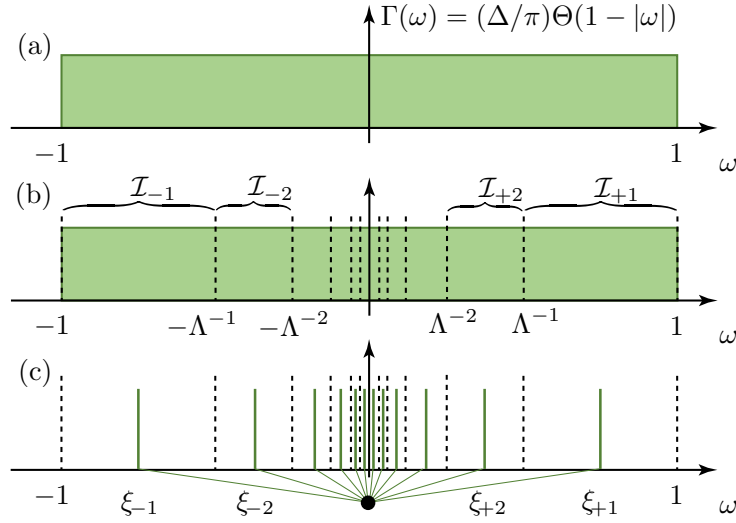


**Fig. 1:** (a) Box-shaped hybridization spectrum  $\Gamma(\omega)$ . (b) Partitioning of the support of  $\Gamma(\omega)$  into logarithmically spaced intervals,  $\mathcal{I}_{\pm n}$ . (c) Hybridization function after logarithmic discretization.

retaining only low-energy states. This procedure yields a set of approximate eigenstates of the Hamiltonian spanning all energy scales of the model. We now discuss these steps one by one.

(i) *Logarithmic discretization:* The bath spectrum, defined on the interval  $\epsilon \in [-1, 1]$ , is discretized on a logarithmic grid. Its grid points are chosen at  $\pm\Lambda^{-n}$ , with  $n = 1, 2, 3, \dots, N$ , where  $\Lambda > 1$  is a discretization parameter, and  $N$  is large enough that  $\Lambda^{-N}$  is smaller than the smallest physical energy scale of interest (e.g.  $T$ ). (In practice, a typical choice is  $\Lambda = 2$ , and  $N$  is chosen such that  $\Lambda^{-N}$  is below machine precision,  $\mathcal{O}(10^{-16})$ .) The grid defines a set of intervals  $\mathcal{I}_{\pm n}$ , defined as  $\mathcal{I}_{+n} = [\Lambda^{-n}, \Lambda^{-n+1}]$  and  $\mathcal{I}_{-n} = [-\Lambda^{-n+1}, \Lambda^{-n}]$  (see Fig. 1(b)). Next, one represents each interval  $\mathcal{I}_{\pm n}$  by a single state, with energy  $\xi_{\pm n}$  and hopping amplitude (to the impurity)  $\gamma_{\pm n}$  (see Fig. 1(c)), and replaces the bath Hamiltonian and hybridization terms by

$$H_{\text{bath}} \rightarrow H_{\text{bath}}^{\text{star}} = \sum_{\pm n, s} \xi_{\pm n} a_{\pm ns}^\dagger a_{\pm ns}, \quad (15a)$$

$$H_{\text{hyb}} \rightarrow H_{\text{hyb}}^{\text{star}} = \sum_{\pm n, s} \gamma_{\pm n} (a_{\pm ns}^\dagger d_s + \text{h.c.}), \quad (15b)$$

where  $a_{\pm ns}$  annihilates the representative bath mode  $\pm n$  with spin  $s$ . This is known as the *star geometry*, because the depiction of the impurity-bath couplings in Fig. 1 is reminiscent of rays emanating from a star. If the discrete bath energies and couplings are chosen as [18],

$$\gamma_{\pm n}^2 = \int_{\mathcal{I}_{\pm n}} d\omega \Gamma(\omega), \quad \xi_{\pm n} = \frac{\int_{\mathcal{I}_{\pm n}} d\omega \Gamma(\omega)}{\int_{\mathcal{I}_{\pm n}} d\omega \Gamma(\omega)/\omega}, \quad (16)$$

then the resulting hybridization spectrum,  $\Gamma^{\text{star}}(\epsilon) = \sum_{\pm n} (\gamma_{\pm})^2 \delta(\epsilon - \xi_{\pm n})$ , serves as a representation of the original  $\Gamma(\epsilon)$  that becomes increasingly good the lower the energy [4]. (More sophisticated choices are available to improve the approximation, see Refs. [19–21].)

(ii) *Wilson chain*: Next, the star geometry is mapped to a chain. To this end, note that in  $H_{\text{hyb}}^{\text{star}}$ , the impurity operator  $d_s$  couples to discretized bath modes only in the combination  $t_d f_{0s}^\dagger = \sum_{\pm n} \gamma_{\pm n} a_{\pm ns}^\dagger$ . ( $t_d$  is chosen such that  $f_{0s}$  obeys  $\{f_{0s}, f_{0s}^\dagger\} = 1$ .) It is therefore advisable to perform a unitary transformation from the  $2N$  discrete modes  $\{a_{\pm n, s}\}$  to a new set of  $\mathcal{L}+1=2N$  orthonormal modes containing  $f_{0s}$ , say  $\{f_{\ell s}\}$ , with  $\ell = 0, 1, 2, \dots, \mathcal{L}$ . This can be achieved by tridiagonalizing the single-particle Hamiltonian matrix for  $H_{\text{bath}}^{\text{star}} + H_{\text{hyb}}^{\text{star}}$ , say  $h^{\text{star}}$ , which has dimensions  $(2N+1) \times (2N+1)$ , using Lanczos tridiagonalization. For example, for  $N = 2$  we obtain

$$h^{\text{star}} = \begin{pmatrix} \xi_{+2} & 0 & \gamma_{+2} & 0 & 0 \\ 0 & \xi_{+1} & \gamma_{+1} & 0 & 0 \\ \gamma_{+2} & \gamma_{+1} & 0 & \gamma_{-1} & \gamma_{-2} \\ 0 & 0 & \gamma_{-1} & \xi_{-1} & 0 \\ 0 & 0 & \gamma_{-2} & 0 & \xi_{-2} \end{pmatrix} \rightarrow h^{\text{chain}} = \begin{pmatrix} 0 & t_d & 0 & 0 & 0 \\ t_d & \epsilon_0 & t_0 & 0 & 0 \\ 0 & t_0 & \epsilon_1 & t_1 & 0 \\ 0 & 0 & t_1 & \epsilon_2 & t_2 \\ 0 & 0 & 0 & t_2 & \epsilon_3 \end{pmatrix}, \quad (17)$$

where the central row and column of  $h^{\text{star}}$  represent the mode  $d_s$ , and the Lanczos scheme is initialized with the vector  $(0, 0, 1, 0, 0)^T$ . Such a tridiagonalization converts  $H_{\text{bath}}^{\text{star}}$  into a form representing a tight-binding chain of  $\mathcal{L}+1$  sites,

$$H_{\text{bath}}^{\text{chain}} = \sum_{\ell=0}^{\mathcal{L}-1} \sum_s t_\ell (f_{\ell s}^\dagger f_{\ell+1, s} + \text{h.c.}) + \sum_{\ell=0}^{\mathcal{L}} \sum_s \epsilon_\ell f_{\ell s}^\dagger f_{\ell s}, \quad (18a)$$

with the impurity  $d$  level (at site  $\ell = -1$ ) coupled to site  $\ell = 0$  with amplitude  $t_d$ :

$$H_{\text{hyb}}^{\text{chain}} = \sum_s t_d (d_s^\dagger f_{0s} + \text{h.c.}). \quad (18b)$$

The corresponding *Wilson chain* representation of the SIAM for a chain with largest site index  $\mathcal{L}$  is given by  $H^\mathcal{L} = H_{\text{loc}} + H_{\text{bath}}^{\text{chain}} + H_{\text{hyb}}^{\text{chain}}$ , with  $H_{\text{loc}}$  given by Eq. (1b).

An important consequence of logarithmic discretization is that the hopping matrix elements  $t_\ell$  and on-site energies  $\epsilon_\ell$  decay exponentially along the chain: the integration intervals  $\mathcal{I}_{\pm n}$  in Eqs. (16) have width  $\Lambda^{-n}(\Lambda-1)$ , thus  $\gamma_{\pm n} \sim \Lambda^{-n/2}$  and  $\xi_{\pm n} \sim \Lambda^{-n}$ , which leads to  $t_\ell \sim \Lambda^{-\ell/2}$  and  $\epsilon_\ell \sim \Lambda^{-\ell}$ . The characteristic energy scale of site  $\ell$  is given by the hopping amplitude onto that site,  $t_{\ell-1} \sim \Lambda^{-(\ell-1)/2}$ . Thus, Wilson chains exhibit *energy scale separation*: different parts of the chain represent different energy scales, with the characteristic energy of site  $\ell$  decreasing exponentially with increasing  $\ell$ .

(iii) *Iterative diagonalization*: The energy scale separation along a Wilson chain can be exploited to numerically diagonalize  $H^\mathcal{L}$  in iterative fashion, adding one site at a time, starting from site  $\ell = 0$ . In doing so, the resolution of the low-energy part of the eigenspectrum will increase exponentially. However, the number of eigenstates will increase exponentially, too. Therefore, a systematic truncation scheme is needed to limit the number of eigenstates that are computed explicitly.

Wilson proposed an energy-based truncation scheme: Suppose that  $H^\ell$  has been diagonalized, yielding a set of eigenstates satisfying  $H^\ell |\alpha\rangle_\ell = E_\alpha^\ell |\alpha\rangle_\ell$ . This set of eigenstates is called *shell*  $\ell$ .

These are divided into two groups: the  $N_{\text{keep}}$  lowest-lying states are *kept*, the remaining ones *discarded*. (Typical choices for  $N_{\text{keep}}$  range between 500 and 5000.) Then a new site,  $\ell+1$ , is added, and  $H^{\ell+1}$  is diagonalized in the direct product space of the new site and the kept states of shell  $\ell$ , whereas the contribution from its discarded states is neglected. Their neglect is justified due to energy scale separation: the energies of the discarded, high-lying states from shell  $\ell$  are significantly larger than the characteristic energy of that shell,  $E_\ell^{\text{high}} \gg \Lambda^{-(\ell-1)/2}$ , which in turn is larger than the coupling to the new site,  $t_\ell = \Lambda^{-\ell/2}$ . The contribution of discarded states on the eigenstates of the new shell  $\mathcal{L}+1$ , estimated by a second-order perturbation argument, is of order  $t_\ell^2/E_\ell^{\text{high}}$ . This is  $\ll (\Lambda^{-\ell/2})^2/\Lambda^{-(\ell-1)/2} = \Lambda^{-(\ell+1)/2}$ , and hence much smaller than the characteristic energy of the new shell,  $\Lambda^{-\ell/2}$ . Therefore, the effect of discarded states can be safely neglected.

For a chain of total length  $\ell$ , Wilson's iterative diagonalization scheme yields a set of  $N_{\text{keep}}$  eigenstates for each shell  $\ell \leq \mathcal{L}$ . In combination, they resolve the spectrum of the Hamiltonian on all energy scales from 1 to  $\Lambda^{-(\mathcal{L}-1)/2}$ . Conceptually, the eigenenergies of shell  $\ell$  represent the low-energy part of the finite-size spectrum of the impurity plus bath put in a spherical box of radius  $R_\ell \sim \Lambda^{(\ell-1)/2}$ , centered on the impurity. As  $\ell$  increases, the box radius increases exponentially, and the finite-size level spacing,  $1/R_\ell \sim \Lambda^{-(\ell-1)/2}$ , decreases exponentially. From an RG perspective, increasing  $R_\ell$  amounts to decreasing the infrared cutoff, here given by the finite-size level spacing, and thus probing the system at lower energy scales. A detailed discussion of this perspective may be found in Refs. [3, 22].

To analyze how the structure of the spectrum changes with  $\ell$ , Wilson defined a set of rescaled excitation energies for each shell,

$$\mathcal{E}_\alpha^\ell = \Lambda^{(\ell-1)/2} (E_\alpha^\ell - E_{\text{GS}}^\ell). \quad (19)$$

These are measured with respect to the ground state (GS) energy of that shell, and scaled such that the spacing of the lowest excitations is  $\mathcal{O}(1)$ . A plot of the rescaled energies  $\mathcal{E}_\alpha^\ell$  versus shell number  $\ell$  on a linear scale, or equivalently, vs. the energy scale  $\Lambda^{-\ell/2}$  on a logarithmic scale, with  $\ell$  increasing in steps of 2, is called an *NRG energy level flow diagram*. It reveals how the rescaled eigenspectra evolve (“flow”) with increasing system size. ( $\ell$  is increased in steps of 2 because of an even-odd effect inherited from  $H_{\text{bath}}^{\text{chain}}$ : its single-particle eigenspectra for  $\mathcal{L}$  even or odd are structurally different, causing the same to be true for the many-body eigenspectra of  $H^\mathcal{L}$ .) An example of an NRG energy level flow diagram is shown in Fig. 2 below.

Once a Wilson chain has been iteratively diagonalized, the approximate eigenstates so obtained can be used to compute physical quantities. These include thermodynamic quantities, such as the impurity entropy  $S(T)$  and spin susceptibility  $\chi(T)$ , but also dynamical, frequency-dependent quantities, such as the dynamic spin susceptibility  $\chi(\omega)$ , or the impurity spectral function,  $\mathcal{A}(\omega)$  and the retarded self-energy,  $\Sigma^R(\omega)$ . For details, see Refs. [23, 24, 17].

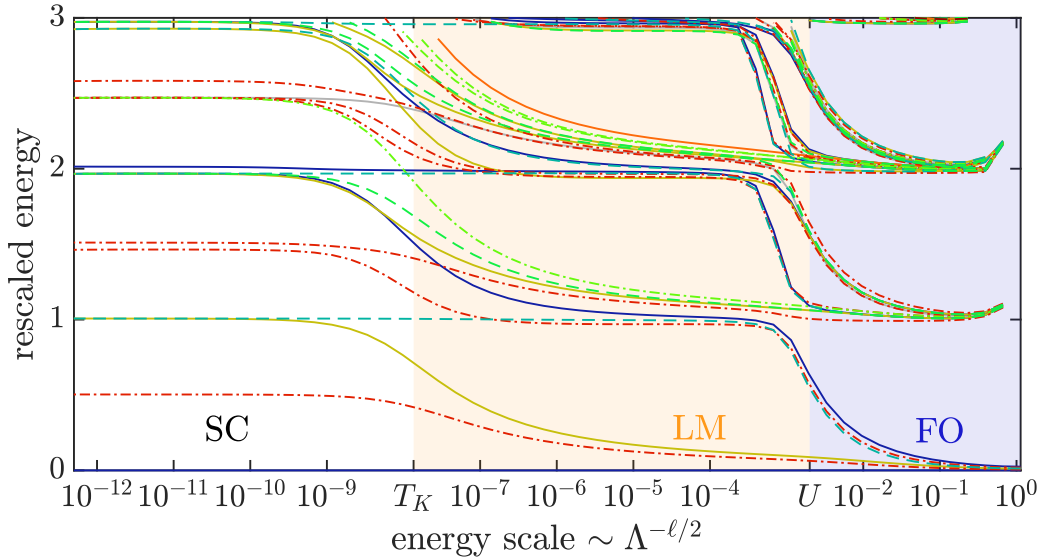


**Fig. 2:** SIAM: NRG energy level flow diagrams (for  $\ell = \text{even}$ ), showing three fixed-point regimes, associated with the free orbital (FO), local moment (LM) and strong-coupling (SC) fixed points.

## 5 NRG results for the single-impurity Anderson model

In the following, we illustrate the RG flow of the SIAM with NRG results. Before we start, let us specify our definition of the Kondo temperature for the SIAM. Following Haldane [25, 26] and Refs. [14, 12], we use

$$T_K = \frac{1}{4\chi(0)} \simeq \sqrt{U\Delta/2} e^{-\pi U/8\Delta + \pi\Delta/2U} e^{x^2}, \quad x = (\varepsilon_d + U/2) \frac{\pi}{\sqrt{2U\Delta}}. \quad (20)$$

The first equality for  $T_K$  corresponds to  $T_{K\chi}$  from our discussion of the spin susceptibility of the Kondo model; the second follows from analytical results for  $\chi(0)$  from the exact Bethe-Ansatz solution of the Anderson model [5]. The parameter  $x$  measures the distance to the particle-hole symmetric point, where  $\varepsilon_d = -U/2$ .

Our numerical results were computed using the following parameters (all energies are given in units of  $D$ ):  $U = 2 \cdot 10^{-3}$ ,  $\varepsilon_d = -U/2 = -10^{-3}$ ,  $\Delta = 0.04U$ , and  $h = 0$  (unless stated otherwise). We are thus in the wide-band limit,  $\Delta, U \ll D = 1$ . The corresponding Kondo temperature from Eq. (20) is  $T_K = 1.3533 \cdot 10^{-8}$ . The numerical NRG parameters were chosen as  $\Lambda = 1.7$ ,  $N_{\text{keep}} = 5000$ .

Figure 2 shows an energy level flow diagram for the SIAM. We observe that there are three energy ranges during which the flow of the finite-size spectrum is almost stationary ( $\ell$  independent). Within each of these,  $\Lambda^{-\ell/2}$  lies within an energy regime governed by one of the RG fixed points of the model. Here, the nomenclature ‘‘fixed point’’ really is appropriate: the spectrum literally remains fixed while changing  $\ell$  (conceptually, increasing the system size  $R_\ell$ ). The energy ranges in between, where the levels shift and/or cross each other, are associated with crossovers between fixed points.

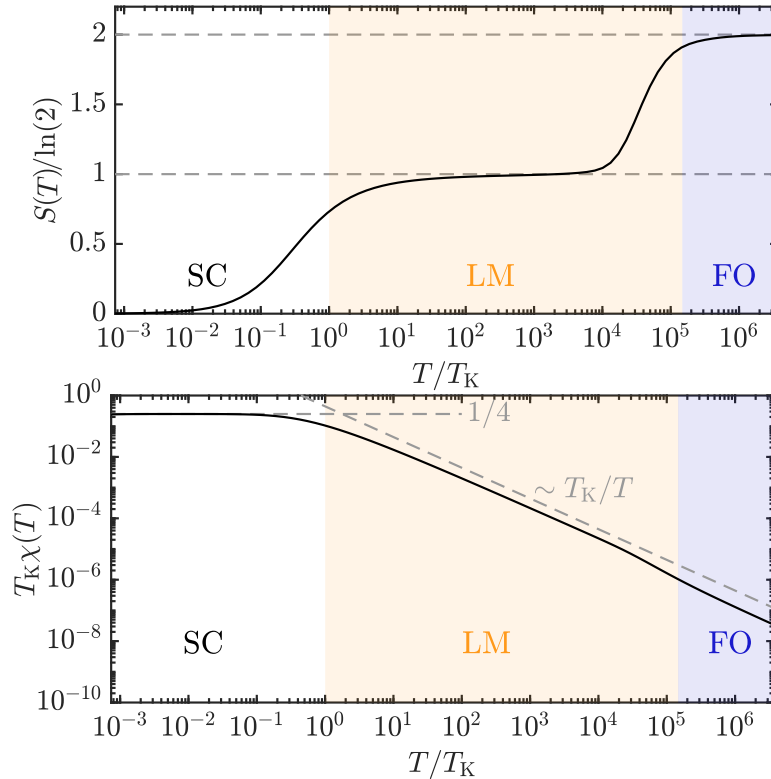


**Fig. 3:** SIAM: Top: Temperature dependence of the impurity entropy,  $S(T)$ . The plateaus at  $\ln(4) = 2 \ln(2)$ ,  $\ln(2)$  and  $\ln(1) = 0$  in the FO, LM and SC regimes, respectively, reflect the number of states that are energetically available to the impurity in these regimes: four ( $|0\rangle$ ,  $|\uparrow\rangle$ ,  $|\downarrow\rangle$ ,  $|\uparrow\downarrow\rangle$ ) in the FO regime, two ( $|\downarrow\rangle$ ,  $|\uparrow\downarrow\rangle$ ) in the LM regime, and one (screened singlet) in the SC regime. Bottom: Temperature dependence of the static spin susceptibility,  $\chi(T)$ . In the LM regime it shows Curie behavior,  $\chi(T) \sim 1/T$ . In the SC regime it saturates at a value,  $\chi(0)$ , which we use as definition for the Kondo temperature, setting  $T_K = 1/(4\chi(0))$ .

For the SIAM, the RG flow has three fixed point regimes (first analyzed with NRG in Refs. [15, 16]), clearly visible in Fig. 2. (I) The *free orbital* (FO) regime involves excitation energies  $\gtrsim U$ . It is governed by “free” (not hindered by  $U$ ) charge fluctuations, arising through real transitions between all four states of the  $d$  level,  $|0\rangle$ ,  $|\uparrow\rangle$ ,  $|\downarrow\rangle$ , and  $|\uparrow\downarrow\rangle$ . (II) The *local moment regime* (LM) involves excitation energies in the range between the Kondo temperature,  $T_K$  and  $U$ . Here, charge fluctuations can occur only virtually, giving rise to spin-flip transitions between  $|\uparrow\rangle$  and  $|\downarrow\rangle$ . Real transitions to  $|0\rangle$  or  $|\uparrow\downarrow\rangle$  are frozen out, since the available excitation energies are too small to overcome the associated cost in Coulomb energy,  $U$ . (III) The *strong-coupling* (SC) regime involves excitation energies well below  $T_K$ . It features a screened spin-singlet, off which Fermi-liquid quasiparticles scatter without spin-flip scattering (cf. the discussion on p. 7). Spin-flip scattering is frozen out, since that would require breaking up the spin singlet, which has binding energy  $\sim T_K$ .

This interpretation of the fixed point spectra is beautifully confirmed by the temperature dependence of two *thermodynamic quantities*, the impurity entropy,  $S(T)$ , and the static local spin susceptibility,  $\chi(T)$ , shown in Fig. 3. As explained in the caption of these plots, both quantities show distinctly different behaviors in the three fixed point regimes, characteristic of a free orbital, a local moment or a screened singlet, respectively.

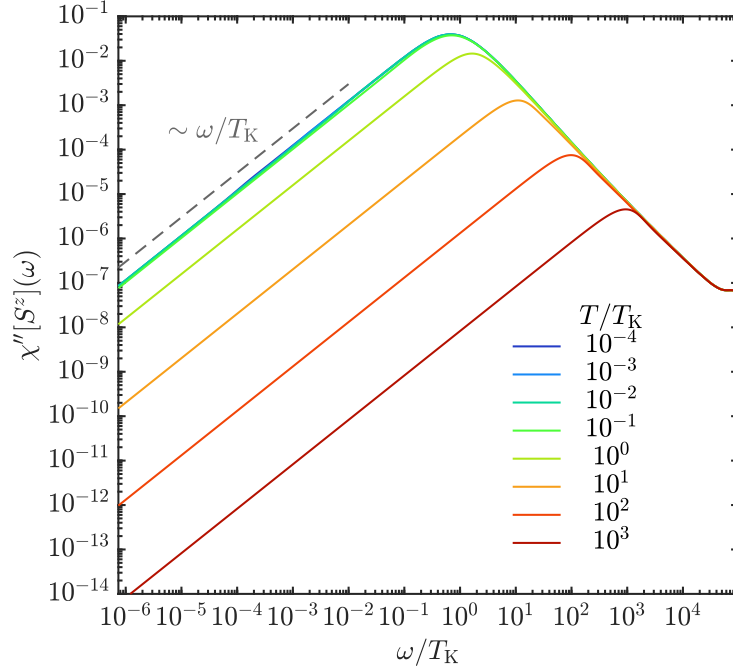


**Fig. 4:** SIAM: Frequency dependence of the imaginary part of the dynamical spin susceptibility,  $\chi''(\omega)$ , plotted on a log-log scale, for a range of different temperatures.

Next, we turn to *dynamical quantities*. First, we consider the dynamical spin susceptibility, defined as

$$\chi(\omega) = \chi'(\omega) + i\chi''(\omega) = \int_{-\infty}^{\infty} dt e^{i\omega t} (-i) \Theta(t) \langle [S^z(t), S^z(0)] \rangle_T. \quad (21)$$

The static spin susceptibility discussed earlier,  $\chi(T)$ , is equal to the zero-frequency limit of the real part here,  $\chi'(\omega = 0)$ . The frequency dependence of the imaginary part,  $\chi''(\omega)$ , is shown in Fig. 4. For  $T = 0$  and  $\omega \gg T_K$ , it increases with decreasing  $\omega$ , characteristic of an almost free spin in the LM regime. It reaches a maximum at  $\omega \simeq T_K$ , where spin screening becomes strong, and for  $\omega \rightarrow 0$  decreases linearly with  $\omega$ . This linear dependence is characteristic of the Fermi liquid behavior of the system in the SC regime (energies  $\ll T_K$ ), and indicative of a well-screened impurity spin. For temperatures  $T \gg T_K$ , the maximum in  $\chi''(\omega)$  occurs at  $T$ , and the peak value of  $\chi''$  decreases with increasing  $T$ . This illustrates how a finite temperature cuts off the RG flow towards strong coupling.

Another dynamical quantity of great interest is the retarded correlator for the  $d$  level,

$$G_s(\omega) = \int_{-\infty}^{\infty} dt e^{i\omega t} (-i) \Theta(t) \langle \{d_s(t), d_s(0)\} \rangle_T = \int d\omega' \frac{\mathcal{A}_s(\omega')}{\omega - \omega' + i0^+}. \quad (22)$$

Specifically, we are interested in its spectral function,  $\mathcal{A}_s(\omega) = -\frac{1}{\pi} \text{Im} G_s(\omega)$ , which characterizes the local density of states associated with the  $d$  level, and in the corresponding retarded self-energy,  $\Sigma_s(\omega)$ , defined via

$$G_s(\omega) = \frac{1}{\omega - \varepsilon_d - \Delta(\omega) - \Sigma_s(\omega)}, \quad (23)$$

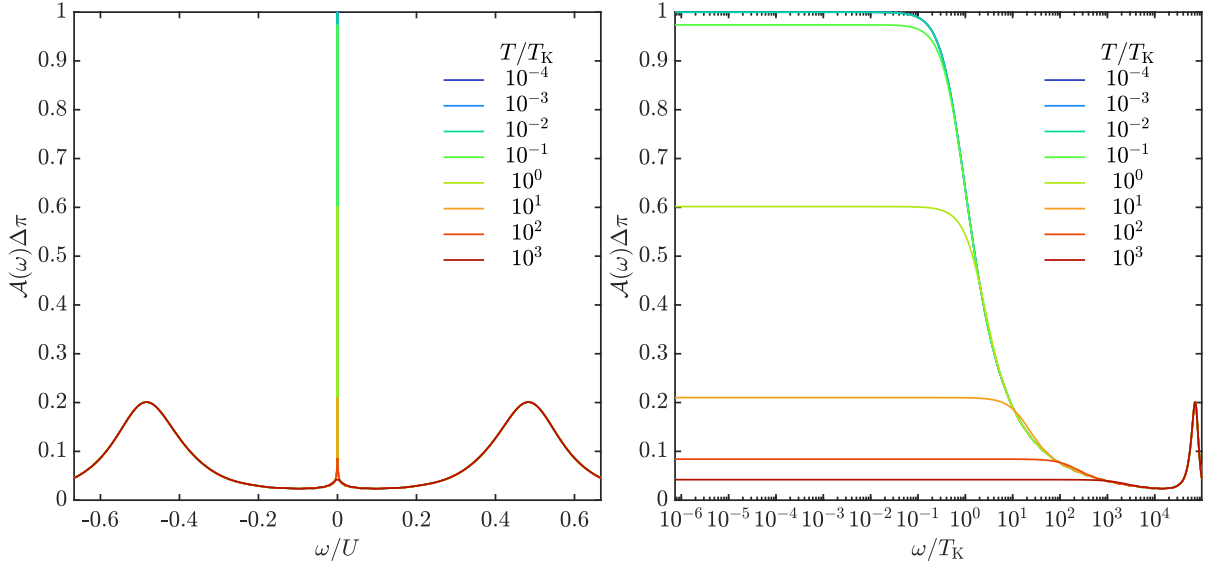


**Fig. 5:** SIAM: Local spectral function,  $A(\omega)$ , for eight different temperatures, shown on a linear scale (left) and a logarithmic scale (right).

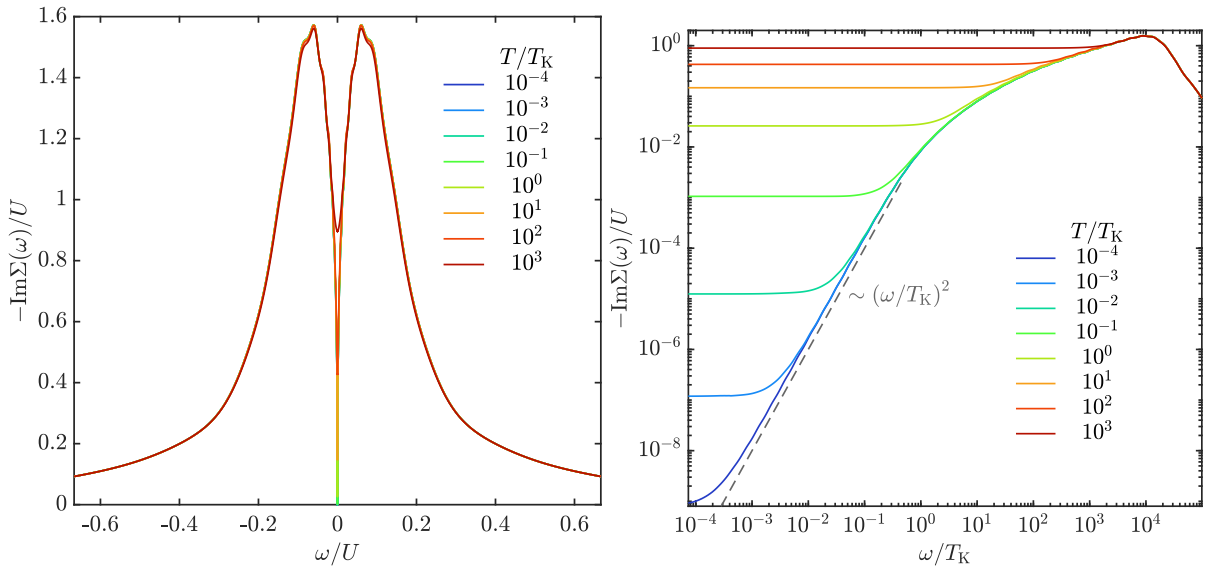


**Fig. 6:** Local self-energy,  $\Sigma(\omega)$ , for eight different temperatures, shown on a linear scale (left) and a logarithmic scale (right).

where  $\Delta(\omega)$  is the *hybridization function* from Eq. (2). Note that  $\Delta(0) = -i\Delta$ , which is why  $\Delta$  sets the hybridization-induced width of the  $d$  level. (For the wide-band limit ( $\Delta, U \ll D$ ) considered here,  $\Delta(\omega) \simeq -i\Delta$  actually holds to very good approximation throughout the regime  $|\omega| \leq U/2$ .) Since we will mostly consider the case  $h = 0$  (no magnetic field), we will henceforth drop the spin index  $s$ .

Figure 5 shows the local spectral function,  $\mathcal{A}(\omega)$ , for a number of different temperatures, ranging from  $T \ll T_K$  to  $T \gg T_K$ . It features two broad peaks at  $\omega = \pm U/2$ , the so-called Hubbard side-bands. These arising from real transitions between the  $d$  level and the band and are essentially independent of  $T$ . Additionally, once  $T$  drops below  $T_K$ ,  $\mathcal{A}(\omega)$  develops a sharp peak at  $\omega = 0$ , known as the *Kondo resonance*. At zero temperature, its width is essentially given

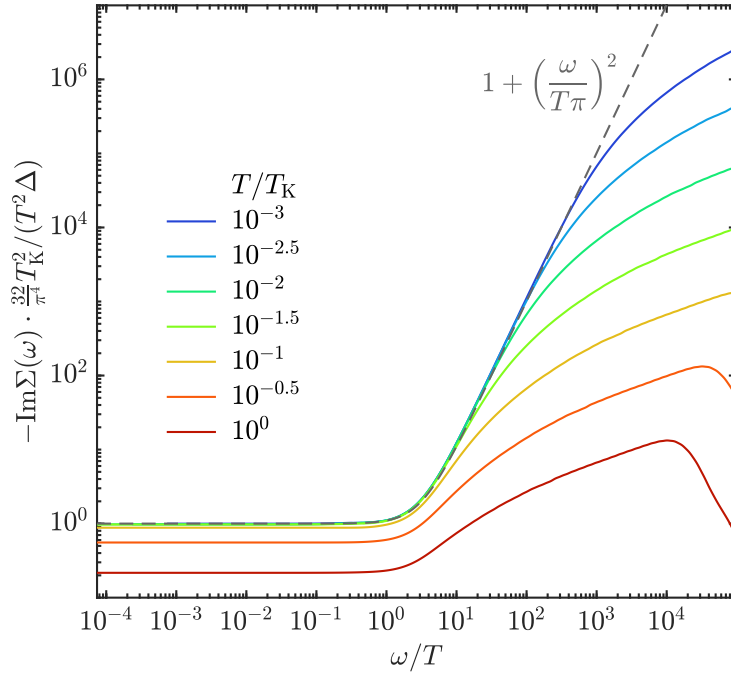


**Fig. 7:** SIAM: Fermi-liquid scaling behavior of the local self-energy,  $\Sigma(\omega, T)$ . For  $\omega, T \ll T_K$ , the rescaled data collapses onto a universal scaling curve in accordance with Eq. (24).

by  $T_K$  and its height is  $\mathcal{A}(0) = 1/(\pi\Delta)$ . The latter relation follows from Eq. (23) by using  $\text{Im}\Sigma(0)|_{T=0} = 0$ , a well-established analytical result that follows from Nozières' Fermi-liquid treatment of the SC regime [13, 14, 12]. Figure 6, which shows the imaginary part of the self-energy,  $-\text{Im}\Sigma(\omega)$ , confirms this fact: At  $T = 0$ , the self-energy indeed drops to zero in the energy range  $|\omega| \ll T_K$ .

The occurrence of the Kondo resonance is perhaps the most striking manifestation of spin screening. Intuitively, it arises because at very low energies,  $\omega, T \ll T_K$ , Fermi-liquid quasiparticles scatter purely elastically off the screened singlet: they acquire a phase shift, but their energy and spin does not change.

When  $\omega$  and/or  $T$  increase from 0, inelastic scattering sets in and  $-\text{Im}\Sigma$  becomes nonzero. As long as  $\omega, T \ll T_K$ , this can still be described using Fermi-liquid theory. By combining known relations from Refs. [27, 12] one finds

$$-\text{Im}\Sigma(\omega, T) = \frac{\pi^2 \Delta (\omega^2 + \pi^2 T^2)}{32 T_K^2}, \quad \omega, T \ll T_K. \quad (24)$$

This implies that a plot of  $-\text{Im}\Sigma(\omega, T)/T^2$  vs.  $\omega/T$  should yield a scaling collapse. Indeed, when the self-energy is computed using state-of-the-art NRG methodology [28, 29], this scaling behavior is beautifully recovered, as shown in Fig. 7.

The application of a local magnetic field  $h$  favors the state  $|\uparrow\rangle$  over  $|\downarrow\rangle$ . It thus tends to polarize the local spin, thereby disrupting spin screening. As a result, the RG flow to strong coupling is cut off at the energy scale  $h$ . This has dramatic consequences for the local spectral function: The Kondo resonances for  $\mathcal{A}_\uparrow(\omega)$  and  $\mathcal{A}_\downarrow(\omega)$  shift apart and get suppressed with increasing field. This behavior is shown in Fig. 8.

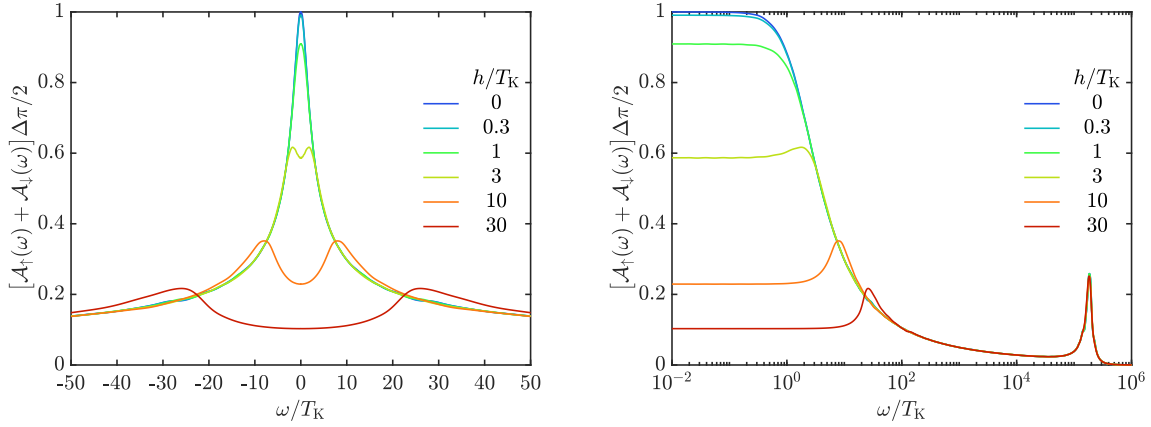


**Fig. 8:** SIAM: Dependence of the local spectral function on magnetic field, computed at  $T = 0$ .

We conclude our discussion of the SIAM by putting it into the context of dynamical mean-field theory (DMFT) [30]. There, one considers a correlated lattice model but assumes the self-energy to be purely local. This allows the model to be mapped onto a quantum impurity model with a hybridization function that has to be determined self-consistently. For the one-band Hubbard model, the corresponding impurity model is the SIAM. DMFT self-consistency then has drastic consequences: at sufficiently high temperature or interaction strength, the Kondo resonance is completely suppressed [31, 32], and the system undergoes a Mott transition from a metallic state to an insulating state.

## 6 Two-channel Kondo model

We end these notes by making a few remarks about a quantum impurity model that does *not* show spin screening: the two-channel Kondo (2CK) model [33]. Its Hamiltonian is similar to that of the usual (one-channel) Kondo model, but now there are two conduction bands, labeled by a channel index  $j = 1, 2$ , that couple symmetrically to the local spin- $\frac{1}{2}$ :

$$H_{2\text{CK}} = \sum_{ks} \sum_{j=1,2} \varepsilon_k \hat{n}_{kjs} + J \hat{\mathbf{S}}_d \cdot \hat{\mathbf{s}}_c, \quad \hat{\mathbf{s}}_c = \sum_{ks, k's'} \sum_{j=1,2} c_{kjs}^\dagger \frac{1}{2} \boldsymbol{\sigma}_{ss'} c_{k'js'} . \quad (25)$$

This model also involves some screening of the local spin by conduction electrons, but full spin-screening is not possible: if the local spin- $\frac{1}{2}$  would form a spin singlet with a Kondo cloud from one channel, that would break channel symmetry. If two Kondo clouds from both channels try to screen the spin- $\frac{1}{2}$  without breaking channel symmetry, they together constitute a spin-1 cloud and *overscreen* the spin- $\frac{1}{2}$ , yielding another spin- $\frac{1}{2}$  object. Repeating this heuristic argument, one concludes that a spin singlet cannot be formed as long as channel symmetry is respected. Therefore, the quasiparticles do not behave as a Fermi liquid—instead, the model shows *non-Fermi-liquid* behavior.

This has striking consequences for physical quantities. Here, we only mention two zero-temperature properties that are decidedly non-Fermi-liquid in character. Figure 9 shows corresponding NRG results.

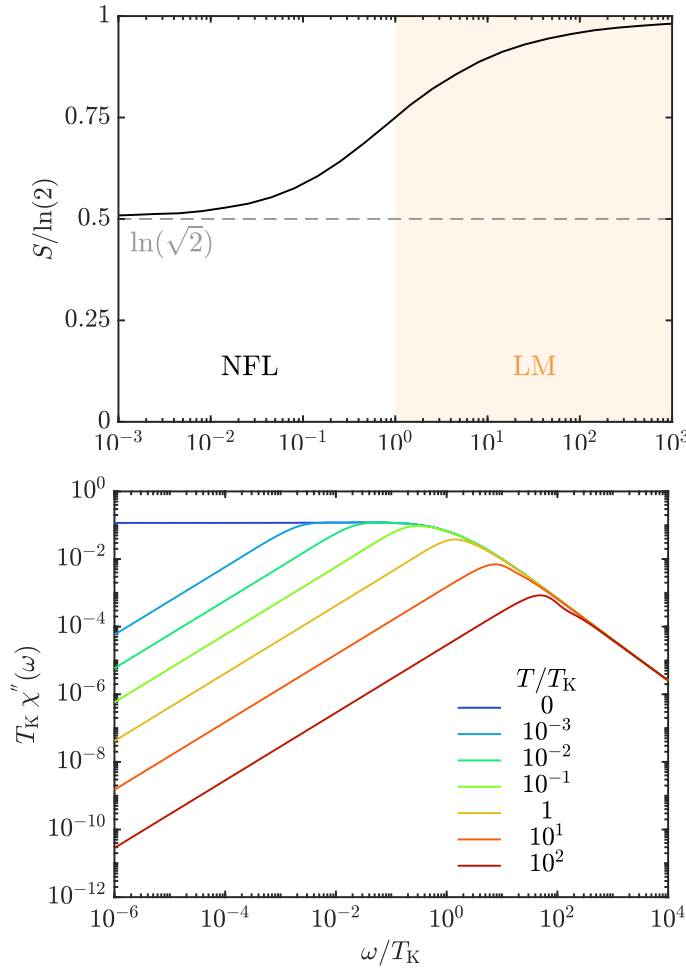


**Fig. 9:** Two-channel Kondo model. *Top:* temperature dependence of the impurity entropy,  $S(T)$ . We defined  $T_K$  through the condition  $S(T_K) = (S(\infty) + S(0))/2$  such that the crossover is centered on  $T_K$ . *Bottom:* Frequency dependence of the imaginary part of the dynamical spin susceptibility,  $\chi''(\omega)$ , plotted on a log-log scale, for a range of different temperatures.

*Impurity entropy:* At  $T = 0$ , the impurity entropy  $S(0)$  does not equal  $\ln(1) = 0$ , but  $\frac{1}{2} \ln(2) = \ln(\sqrt{2})$ . The unusual fractional prefactor reflects the fact that the impurity retains some dynamical character, since it is not fully screened.

*Dynamical spin susceptibility:* At  $T = 0$ , the imaginary part of the susceptibility approaches a constant as  $\omega \rightarrow 0$ ,  $\chi''(\omega) \sim \text{const}$  (in contrast to the Fermi liquid behavior,  $\chi''(\omega) \sim \omega$ , of the one-channel Kondo model). That, in turn, implies that the real part diverges logarithmically,  $\chi'(\omega) \sim \ln(T_K/\omega)$ . This, too, indicates that the impurity is not fully screened but retains some dynamical character, even at  $T = 0$ .

### Acknowledgement

I warmly thank Andreas Gleis and Jeongmin Shim for doing the NRG computations reported in these notes and creating the corresponding figures, and Andreas Gleis for establishing Eq. (24).

## A Schrieffer-Wolff transformation

The KM can be obtained from the SIAM using a Schrieffer-Wolff transformation [11] and a projection onto the subspace where  $n_d = 1$ . Here, we briefly outline the key steps of this derivation. The starting point is the SIAM Hamiltonian, written in the form  $H_{\text{SIAM}} = H_0 + H_1$ , with  $H_0 = H_{\text{bath}} + H_{\text{loc}}$  being  $\mathcal{O}(v^0)$  and  $H_1 = H_{\text{hyb}}$  being  $\mathcal{O}(v^1)$ , where  $v = v_k$  is the hybridization parameter. The goal is to find a unitary transformation such that the new Hamiltonian,  $\tilde{H} = e^A H_{\text{SIAM}} e^{-A}$ , contains no terms of order  $\mathcal{O}(v^1)$ . Here,  $A$  is anti-unitary,  $A^\dagger = -A$ , with an hybridization expansion of the form  $A = \mathcal{O}(v^1) + \mathcal{O}(v^2) + \dots$ . Expanding  $\tilde{H}$  in powers of  $A$  using the Baker-Campbell-Hausdorff formula, one obtains

$$\tilde{H} = (H_0 + H_1) + [A, H_0 + H_1] + \frac{1}{2}[A, [A, H_0 + H_1]] + \mathcal{O}(v^3) \quad (26)$$

(The term slashed out is  $\mathcal{O}(v^3)$ .) To ensure that the right side contains no terms  $\mathcal{O}(v^1)$ , we must choose  $A$  such that  $H_1 = -[A, H_0]$ , implying

$$\tilde{H} = H_0 + \frac{1}{2}[A, H_1] + \mathcal{O}(v^3). \quad (27)$$

One may readily verify that the requirement  $H_1 = -[A, H_0]$  is satisfied by

$$A = \sum_{ks} v \left( \frac{1}{\varepsilon_k - \varepsilon_d} c_{ks}^\dagger d_s + \frac{U}{(\varepsilon_d - \varepsilon_k)(\varepsilon_d + U - \varepsilon_k)} d_{-s}^\dagger d_{-s} c_{ks}^\dagger d_s \right) - \text{h.c.} \quad (28)$$

Inserting this into Eq. (27) and dropping terms that are zero in the subspace where  $n_d = 1$ , one obtains

$$\tilde{H}|_{n_d=1} = \sum_{ks} \varepsilon_k \hat{n}_{ks} + \sum_{kk'} \tilde{v}_{kk'} \hat{\mathbf{S}}_d \cdot c_{ks}^\dagger \frac{1}{2} \boldsymbol{\sigma}_{ss'} c_{k's'} + \dots \quad (29)$$

where the coupling matrix elements are given by

$$\tilde{v}_{kk'} = \frac{-\frac{1}{2}v^2 U}{(\varepsilon_d - \varepsilon_k)(\varepsilon_d + U - \varepsilon_k)} + (k \leftrightarrow k'). \quad (30)$$

In Eq. (29), the ellipsis  $\dots$  stands for terms of the form  $\sum_{kk'} c_{ks}^\dagger c_{k's}$ , describing potential scattering, i.e., scattering without any spin dependence. These are usually ignored when discussing the Kondo effect, because in contrast to the spin-exchange interaction of the second term in Eq. (29), they do *not* give rise to a logarithmic temperature dependence when treated perturbatively. In renormalization group (RG) terminology, spin-exchange is a relevant perturbation, whereas potential scattering is not.

Now consider low-energy excitations close to the Fermi energy, then  $\tilde{v}_{kk'}$  simplifies to

$$\tilde{v}_{kk'} \simeq -\frac{v^2 U}{\varepsilon_d (\varepsilon_d + U)} = J, \quad \forall |\varepsilon_k|, |\varepsilon_{k'}| \ll |\varepsilon_d|, |\varepsilon_d + U|. \quad (31)$$

In this limit,  $\tilde{H}$  of Eq. (29) thus reduces to the Kondo Hamiltonian  $H_{\text{KM}}$  of Eq. (7), with an exchange coupling constant  $J$  given by Eq. (31). Note that this equals the expression for  $J$  given in Eq. (6) above, found by considering 2nd order spin-flip processes.

To summarize the above discussion: the low-energy behavior of the SIAM, at energy scales for which charge fluctuations involving  $|0\rangle$  and  $|\uparrow\rangle$  are "frozen out" (can occur only virtually), is described by the KM.

## References

- [1] W.J. de Haas, J. de Boer, and G.J. van den Berg, *Physica* **1**, 1115 (1934)
- [2] J. Kondo, *Prog. Theor. Phys.* **32**, 37 (1964)
- [3] K.G. Wilson, *Rev. Mod. Phys.* **47**, 773 (1975)
- [4] R. Bulla, T.A. Costi, and T. Pruschke, *Rev. Mod. Phys.* **80**, 395 (2008)
- [5] A. Tsvelick and P. Wiegmann, *Adv. Phys.* **32**, 453 (1983)
- [6] N. Andrei, K. Furuya, and J.H. Lowenstein, *Rev. Mod. Phys.* **55**, 331 (1983)
- [7] I. Affleck and A. Ludwig, *Nucl. Phys. B* **352**, 849 (1991)
- [8] V.J. Emery and S. Kivelson, *Phys. Rev. B* **46**, 10812 (1992)
- [9] G. Zaránd and J. von Delft, *Phys. Rev. B* **61**, 6918 (2000)
- [10] E. Gull, A.J. Millis, A.I. Lichtenstein, A.N. Rubtsov, M. Troyer, and P. Werner, *Rev. Mod. Phys.* **83**, 349 (2011)
- [11] J.R. Schrieffer and P.A. Wolff, *Phys. Rev.* **149**, 491 (1966)
- [12] M. Filippone, P. Moca, A. Weichselbaum, J. von Delft, and C. Mora, *Phys. Rev. B* **98**, 075404 (2018)
- [13] P. Nozières, *J. Low Temp. Phys.* **17**, 31 (1974)
- [14] C. Mora, C.P. Moca, J. von Delft, and G. Zaránd, *Phys. Rev. B* **92**, 075120 (2015)
- [15] H.R. Krishna-murthy, J.W. Wilkins, and K.G. Wilson, *Phys. Rev. B* **21**, 1003 (1980)
- [16] H.R. Krishna-murthy, J.W. Wilkins, and K.G. Wilson, *Phys. Rev. B* **21**, 1044 (1980)
- [17] A. Weichselbaum, *Phys. Rev. B* **86**, 245124 (2012)
- [18] J. Vivaldo L. Campo and L.N. Oliveira, *Phys. Rev. B* **72**, 104432 (2005)
- [19] R. Žitko, *Comp. Phys. Commun.* **180**, 1271 (2009)
- [20] R. Žitko and T. Pruschke, *Phys. Rev. B* **79**, 085106 (2009)
- [21] B. Bruognolo, N.O. Linden, F. Schwarz, S.S.B. Lee, K. Stadler, A. Weichselbaum, M. Vojta, F.B. Anders, and J. von Delft, *Phys. Rev. B* **95**, 121115 (2017)
- [22] J. von Delft, G. Zaránd, and M. Fabrizio, *Phys. Rev. Lett.* **81**, 196 (1998)
- [23] R. Peters, T. Pruschke, and F.B. Anders, *Phys. Rev. B* **74**, 245114 (2006)

- 
- [24] A. Weichselbaum and J. von Delft, Phys. Rev. Lett. **99**, 076402 (2007)
  - [25] F.D.M. Haldane, Phys. Rev. Lett. **40**, 416 (1978)
  - [26] F.D.M. Haldane, J. Phys. C: Solid State Phys. **11**, 5015 (1978)
  - [27] A.C. Hewson, J. Phys.: Condens. Matter **13**, 10011 (2001)
  - [28] F.B. Kugler, Phys. Rev. B **105**, 245132 (2022)
  - [29] A. Gleis (unpublished) (2022)
  - [30] A. Georges, G. Kotliar, W. Krauth, and M.J. Rozenberg, Rev. Mod. Phys. **68**, 13 (1996)
  - [31] R. Bulla, Phys. Rev. Lett. **83**, 136 (1999)
  - [32] R. Bulla, T.A. Costi, and D. Vollhardt, Phys. Rev. B **64**, 045103 (2001)
  - [33] P. Nozières and P. Blandin, J. Phys. **41**, 193 (1980)